Fibrous Hybrid of Graphene and Sulfur Nanocrystals for High-Performance Lithium–Sulfur Batteries

Guangmin Zhou,[†] Li-Chang Yin,[†] Da-Wei Wang,[‡] Lu Li,[†] Songfeng Pei,[†] Ian Ross Gentle,[‡,§] Feng Li,[†,*] and Hui-Ming Cheng[†,*]

[†]Shenyang National Laboratory of Materials Science, Institute of Metal Research, Chinese Academy of Sciences, 72 Wenhua Road, Shenyang 110016, China, [‡]ARC Centre of Excellence for Functional Nanomaterials, AIBN, The University of Queensland, Brisbane, Qld 4072, Australia, and [§]School of Chemistry and Molecular Biosciences, The University of Queensland, Brisbane, Qld 4072, Australia

ABSTRACT Graphene–sulfur (G–S) hybrid materials with sulfur nanocrystals anchored on interconnected fibrous graphene are obtained by a facile one-pot strategy using a sulfur/carbon disulfide/alcohol mixed solution. The reduction of graphene oxide and the formation/binding of sulfur nanocrystals were integrated. The G–S hybrids exhibit a highly porous network structure constructed by fibrous graphene, many electrically conducting pathways, and easily tunable sulfur content, which can be cut and pressed into pellets to be directly used as lithium–sulfur battery cathodes without using a metal current-collector, binder, and conductive additive. The porous network and sulfur nanocrystals enable rapid ion transport and short Li^+ diffusion distance, the interconnected fibrous graphene provides highly conductive electron transport pathways, and the oxygen-containing (mainly hydroxyl/epoxide) groups show strong binding with polysulfides, preventing their dissolution into the electrolyte based on first-principles calculations. As a result, the G–S hybrids show a high capacity, an excellent high-rate performance, and a long life over 100 cycles. These results demonstrate the great potential of this unique hybrid structure as cathodes for high-performance lithium–sulfur batteries.

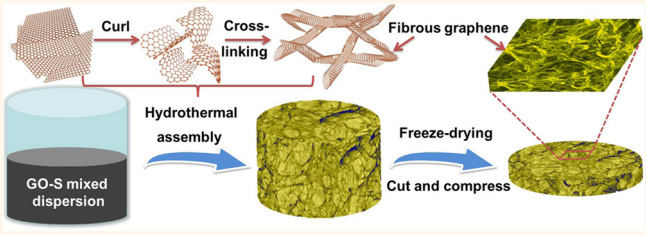

KEYWORDS: graphene · sulfur nanocrystal · hybrid · oxygen functional group · energy storage · lithium–sulfur battery

The development of high-capacity energy storage systems is highly desirable from the viewpoint of both energy and environmental issues. Lithium–sulfur (Li–S) batteries have attracted great interest as potential energy storage devices for electrical vehicles and other applications needing large-scale electricity storage because of their high theoretical energy density of 2567 W h kg^{-1}, which is more than 5 times that of lithium ion batteries based on conventional insertion compound cathodes.[1–3] Other advantages are that elemental sulfur is low cost, has low toxicity, and is an abundant resource. However, the practical application of Li–S batteries is greatly hampered by two major challenges including (i) high solubility of the reaction polysulfide products, which can shuttle between the anode and cathode, forming deposits of solid Li_2S_2 and Li_2S on the cathode, causing loss of the active material, which leads to low Coulombic efficiency, low utilization of the sulfur cathode, and a severe degradation of cycle life, and (ii) the low electrical conductivity of sulfur, the intermediate polysulfide products, and the final Li_2S, affecting the reaction rate of the battery.[4–6]

Some strategies have been proposed to alleviate the impact of the polysulfide shuttle. For instance, extensive studies have been carried out to improve the electrical conductivity of the sulfur electrode and to confine the sulfur and polysulfides in a carbon matrix. For example, ordered mesoporous carbon,[1,7] hierarchical porous carbon,[8,9] microporous carbon spheres,[10] hollow carbon spheres,[11,12] carbon nanotubes/nanofibers,[13,14] and graphene[15–18] have been investigated as the confining/conductive medium and have shown improved cyclic stability. Among these carbonaceous materials, graphene has opened new possibilities and is promising as a two-dimensional (2D) conductive support because of its high electrical conductivity, superior mechanical flexibility, high chemical and thermal stability, high surface functionality, and large

* Address correspondence to cheng@imr.ac.cn, fli@imr.ac.cn.

Received for review March 11, 2013 and accepted May 14, 2013.

Published online May 14, 2013
10.1021/nn401228t

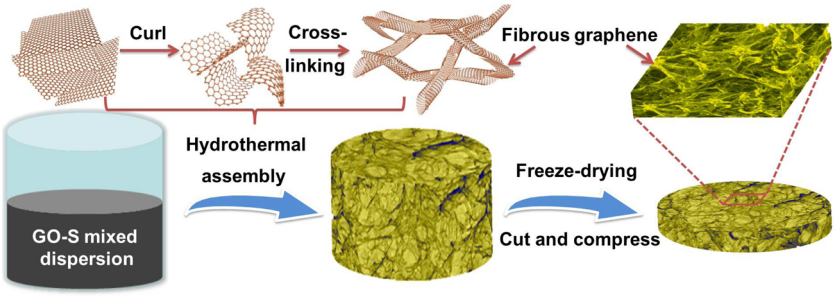

Figure 1. Illustration of the formation process of the G−S hybrid and schematic of fabrication of a self-supporting electrode.

surface area.[19,20] Moreover, reduction of graphene oxide (GO) provides a way to produce graphene on a large scale for practical applications.[21] However, graphene layers are prone to agglomerate during the reduction and drying process because of strong $\pi-\pi$ stacking and hydrophobic interactions. Consequently, many unique properties of graphene are significantly compromised or even unavailable.[22] Self-assembly of graphene into macroscopic materials can translate the intriguing properties of graphene into the resulting macrostructures for practical applications.[23,24] When used as electrodes, these well-defined interpenetrating structures provide macroscopic graphene materials with a large surface area, high mechanical strength, and fast mass and electron transport due to the combination of a porous structure and excellent intrinsic properties of graphene.[25−28]

It is worth noting that the surface chemistry of carbonaceous materials has been recently recognized as another important aspect affecting the performance of Li−S batteries. For example, Tarascon's group found that using oxygenated porous structures can improve the capacity retention of sulfur cathodes, which might be due to weak binding between the polysulfides and the oxygenated framework.[29] Zhang's group showed that the oxygen-containing groups on GO could immobilize sulfur in the cathode material of Li−S cells.[30,31] However, little attention has been paid to the chemical interaction of polysulfides with graphene, which is worthy of consideration because sulfur is converted to polysulfide ions during the charge/discharge processes. Progress in this field has inspired us to study the interaction mechanism between polysulfide species and oxide-containing surfaces, in the hope that it will facilitate understanding of the reversibility and long cyclic stability of sulfur electrodes.

Herein, we have prepared a cathode that is a self-supporting fibrous graphene−sulfur (G−S) hybrid with good electrical conductivity. We developed a one-pot strategy using the hydrothermal reduction of GO and its self-assembly with sulfur nanocrystals precipitated from a sulfur/carbon disulfide (CS_2)/alcohol mixed solution. This method has the merit of easy control over the amount of sulfur, uniform distribution of the sulfur nanocrystals, and tight contact of the sulfur with graphene. It can be cut and pressed into plates for direct use as Li−S battery electrodes without a metal current-collector, binder, and conductive additive, as illustrated in Figure 1. The fibrous graphene facilitates electron transfer, porous network resulting from the interconnected graphene allows for rapid ion transport, and the sulfur nanocrystals provide short Li^+ diffusion distances. Our experimental observations, combined with first-principles calculations, demonstrate that the dissolution/diffusion of polysulfide anions in the electrolyte can be greatly reduced by the strong binding of sulfur to the oxygen-containing (mainly hydroxyl/epoxide) groups on reduced graphene oxide, resulting in improved cyclic stability.

RESULTS AND DISCUSSION

Figure 2a shows typical photographs of the as-prepared materials. Sample I, made from GO and sulfur as precursors without the addition of a CS_2 solution, shows a rough surface, and yellow sulfur agglomerates can be clearly observed on the surface of the G−S mixture (G−S_{mix}). In contrast, for samples II to IV, the G−S assembled hybrids fabricated from GO, sulfur-dissolving CS_2 (adding 100, 150, and 200 mg of sulfur, respectively), and alcohol dispersion show a smooth surface, and their volume is almost independent of sulfur loading. The sulfur contents in samples II−IV are 55, 63, and 71 wt % according to thermogravimetric analysis (TGA, Figure S1, denoted as G−S55, G−S63, and G−S71). These results indicate that the alcohol acts to improve the miscibility of the sulfur/CS_2 and the GO aqueous solution and plays an important role in the formation of homogeneous G−S hybrids. GO is also an important precursor because if we synthesize G−S hybrids from intercalation-exfoliated graphene with a very small amount of oxygen functional groups (C/O = 38.9) and from thermally exfoliated reduced graphene with a medium amount of oxygen functional groups (C/O = 10.6) after the hydrothermal process with the same amount of sulfur in the mixed solution (see Experimental Section), only G−S hybrids (powder) were obtained (Figure S2a). After freeze-drying, the G−S hybrids (powder) were collected and the weight percentage of sulfur in the hybrid powder tested by TGA was 60 and 59 wt % (Figure S2b, denoted as G−S60 hybrid (powder) and G−S59 hybrid (powder)).

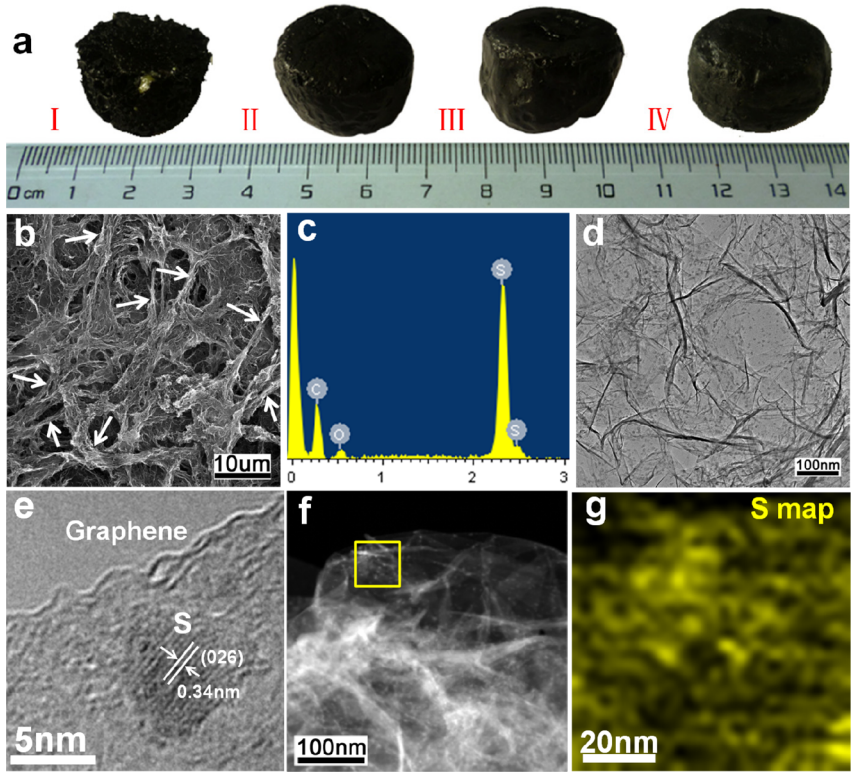

Figure 2. (a) Photographs of the as-prepared (I) G−S_{mix} using GO and sulfur as precursors without adding CS_2 and (II−IV) G−S hybrids with sulfur loadings of 55, 63, and 71 wt % using GO, sulfur-dissolving CS_2, and alcohol dispersion as precursors, after hydrothermal treatment at 180 °C for 10 h. (b) SEM image of the interconnected fibrous microstructure of the G−S63 hybrid and (c) its corresponding EDS spectrum (unit: keV). (d) TEM and (e) HRTEM images of the G−S63 hybrid. (f) STEM image and (g) corresponding sulfur map of the region indicated by the yellow square in (f) of the G−S63 hybrid.

The G−S hybrid materials have an interconnected porous network resulting from the fibrous graphene, as shown in Figure 2b (marked by the white arrows) and Figure S3. The width of the fibrous graphene is 1−2 μm, and the porous network consists of stacked graphene flakes, indicating that GO sheets were rolled up into a cross-linking fibrous structure during the hydrothermal process (Figure 1). In contrast, the scanning electron microscopy (SEM) image of the G−S_{mix} (sample I) shows strongly aggregated graphene with a loose structure and many large pores (several tens of micrometers in diameter, Figure S4). Energy-dispersive X-ray spectroscopy (EDS) reveals the presence of C, O, and S in the G−S63 hybrid (Figure 2c). Figure 2d and Figure S5 show the transmission electron microscopy (TEM) images of the G−S hybrids, in which sulfur nanocrystals with a particle size in the range of 5−10 nm are uniformly distributed on the surface of graphene. It is worth noting that even after strong ultrasonication to disperse samples for TEM characterization, the sulfur nanocrystals are still anchored to the surface of the graphene with a high surface concentration, suggesting a strong interaction between graphene and sulfur. The high-resolution TEM (HRTEM) image in Figure 2e shows the edge of a graphene sheet with a tightly anchored sulfur nanocrystal. The adjacent fringe spacing of the aligned lattice fringes was about 0.34 nm, corresponding to the (026) plane of sulfur. A scanning TEM (STEM) image (Figure 2f) and corresponding sulfur map (Figure 2g) of the region indicated in Figure 2f provide additional evidence to confirm the homogeneous distribution of sulfur on the surface of graphene. However, the sulfur tends to spontaneously agglomerate and form several micrometer-size particles on the intercalation-exfoliated graphene with a very small oxygen content (Figure S6a,b). As for the thermally exfoliated reduced graphene with a moderate oxygen content, the sulfur particles show a size of several tens to several hundreds of nanometers (Figure S6c,d). These results suggest that the presence of oxygen-containing functional groups plays an important role in anchoring and preventing the sulfur from growing into bulk crystalline particles.[32,33]

X-ray diffraction (XRD) patterns of the G−S hybrids are shown in Figure S7. The hybrids exhibit a broad diffraction peak at around 25°, confirming the reduction of GO with irregular layer stacking during the hydrothermal reaction. The sulfur shows sharp and strong peaks indicating a well-defined crystal structure, which is consistent with the TEM analysis. To elucidate the extent of the binding between the graphene and sulfur nanocrystals, X-ray photoelectron spectroscopy (XPS) measurements were performed. Gaussian fits to the C 1s spectra of GO and the G−S63 hybrid both show four peaks, but in different ratios. The C 1s signal of GO in

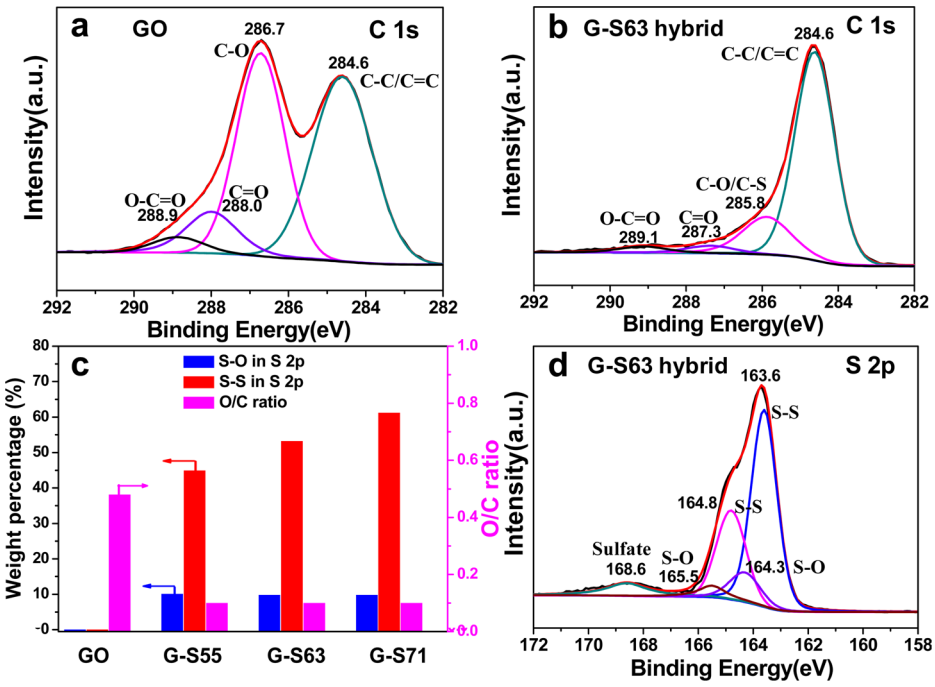

Figure 3. C 1s XPS spectra of the (a) GO and (b) G−S63 hybrid. (c) Relationship of the O/C ratio and weight percentage of S−O, S−S in S 2p in the GO, G−S55, G−S63, and G−S71. (d) S 2p XPS spectrum of the G−S63 hybrid.

Figure 3a consists of component peaks at 284.6, 286.7, 288.0, and 288.9 eV, corresponding to carbon species of C−C/C═C, C−O, C═O, and O−C═O, respectively.[34] After hydrothermal treatment, the hydroxyl and epoxide peaks were greatly reduced, as were those for the carbonyl and carboxyl groups to a lesser extent, while the peak corresponding to the sp^2 carbon increased and became narrower. This indicates that these oxygen-containing functional groups are removed and converted to C−O−S bonds during the reduction−assembly process (Figure 3b). Meanwhile, the shifts in the binding energies of carbon bonded to oxygen (such as C−O and C═O) compared to GO suggest a different chemistry. The O 1s spectrum of the G−S63 hybrid (Figure S8) can be deconvoluted into three peaks. The peak at 531.2 eV is assigned to C═O groups, and the peak at 533.3 eV is ascribed to C−OH and/or C−O−C groups (hydroxyl and/or epoxide).[32,35] The peak centered at 532.0 eV is attributed to the formation of an S−O bond.[31,36] The O/C ratios are 0.48 and 0.10 for the GO and G−S hybrids, which also implies the partial reduction of GO in the hybrids (Figure 3c). In the S 2p spectrum of the G−S63 hybrid (Figure 3d), the S $2p_{3/2}$ (163.6 and 164.8 eV) and $2p_{1/2}$ (164.3 and 165.5 eV) spin−orbit levels with an energy separation of 1.2 eV are attributed to the S−S bond and S−O species, respectively.[29,31] With the increase of sulfur loading, the proportion of S−S increases, while S−O in S 2p is similar for G−S55, G−S63, and G−S71 hybrids (Figure 3c). The other small peak at 168.6 eV can be ascribed to the sulfate species formed by the oxidation of sulfur in air.[37] The above analysis indicates that the sulfur nanocrystals maintain intimate contact with graphene through S−O bonding, which could immobilize sulfur and the corresponding polysulfides produced during the discharge/charge process, preventing the loss of active materials and stabilizing the cyclic life of Li−S batteries.

To better understand the possible functionality of oxygen-containing groups on the performance of Li−S batteries during cycling, especially for the polysulfides produced, we performed density functional theory (DFT) calculations to explore the interaction between oxygen-containing species and polysulfides. On the basis of the above experimental results, the residual oxygen-containing functional groups on graphene are mainly hydroxyl and epoxide, which is in accordance with the recent theoretical prediction.[38] Here, we focused on S_3 clusters and multiply charged S_3 anions (monoanion, S_3^- and dianion, S_3^{2-}) with a chain-like structure, since other multiply charged S anions ($S_n^{\sigma-}$, $n = 4-8$, $\sigma = 1, 2$) take chain-like structures based on DFT studies[39,40] and should behave similarly to S_3 anions on a graphene surface. Smaller sulfur molecules (S_{2-4}) were also reported with good electrochemical performance in Li−S batteries recently.[41] Figure 4a presents the fully relaxed geometric structures of the neutral S_3 clusters and polyanions (S_3^- and S_3^{2-}). The calculated S−S bond length and bond angle of S_3^- are almost the same as those of S_3^{2-} and are respectively longer and smaller than those for a neutral S_3 cluster. The longer S−S bond length and reduced bond angle of S_3^{1-} and S_3^{2-} are the result of a charge redistribution, as shown in Figure 4a. For example, the two terminal sulfur atoms are negatively charged (−0.14 e) while the center sulfur atom is positively charged (+0.28 e) for a

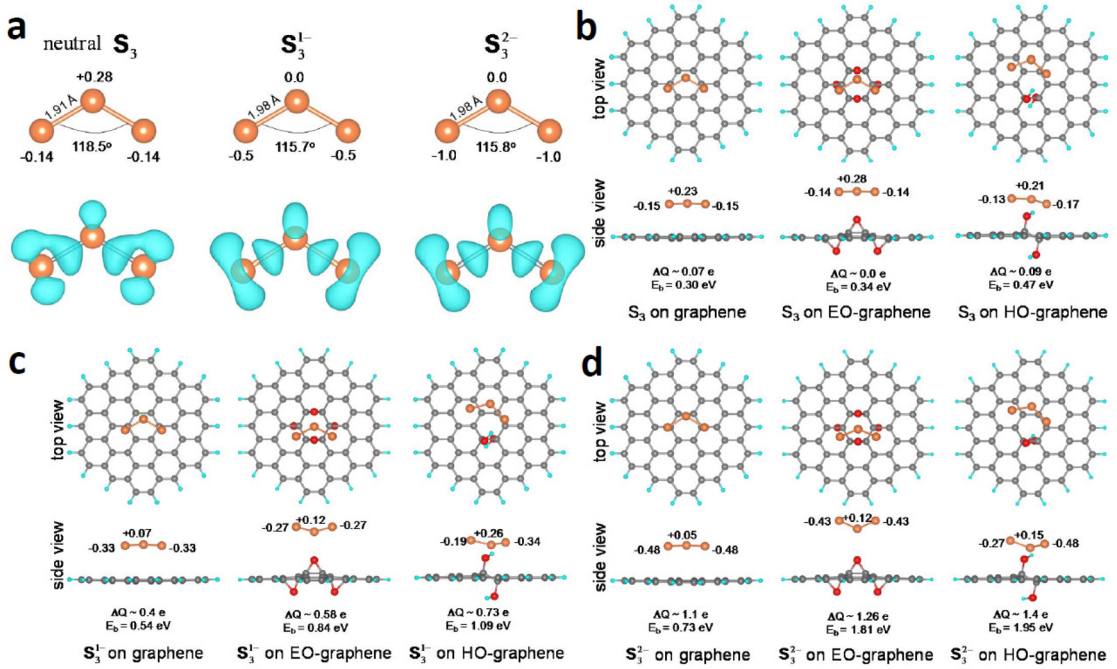

Figure 4. (a) Geometric structures of a fully relaxed neutral S_3 and charged S_3^- (S_3^{2-}) clusters and corresponding charge density plots with a charge isocontour of 0.002 e/Å^3 (lower panel). Side and top view of (b) a neutral S_3 cluster, (c) S_3^-, and (d) S_3^{2-} on graphene, EO-graphene, and HO-graphene surfaces. S, C, O, and H atoms are represented by orange, dark gray, red, and small cyan balls. The calculated charge population for each sulfur atom, the binding energy (E_b), and corresponding charge transfer (ΔQ) are also shown.

neutral S_3 cluster; however, in the case of S_3^- (S_3^{2-}), two terminal sulfur atoms are more negatively charged, −0.5 e (−1.0 e), while the center sulfur atom remains in a neutral state. In order to compare the interaction between a charged S_3 cluster (S_3^- and S_3^{2-}) and graphene with that between a neutral S_3 cluster and graphene, we define the binding energy (E_b) as follows:

$$E_b = E(S_3^{\sigma}@\text{graphene}) - E(\text{graphene}) - E(S_3^{\sigma})$$
$$\sigma = 0, -1, \text{and } -2$$

Here, E(graphene), $E(S_3^{\sigma})$, and $E(S_3^{\sigma}@\text{graphene})$ are total energies of graphene, an isolated S_3 cluster, and graphene bound to a S_3 cluster, respectively. Using the above definition, we observe a moderate binding effect (0.30 eV) between a neutral S_3 cluster and the pristine graphene surface, which slightly increases to 0.34 (0.47) eV after introducing epoxide (hydroxyl) groups on the graphene surface, EO-graphene (HO-graphene), as described in Figure 4b. This implies that epoxide and hydroxyl groups remaining on the graphene surface do not greatly improve the binding between graphene and a neutral S_3 cluster. However, as shown in Figure 4c and d, hydroxyl and epoxide groups can remarkably increase the binding between graphene and the charged S_3 clusters (S_3^- and S_3^{2-}). For example, the binding energy of S_3^- (S_3^{2-}) on the HO-graphene is calculated to be 1.09 (1.95) eV, which is about 2−3 times larger than that of S_3^- (S_3^{2-}) on the pristine graphene surface. Charge population analysis indicates that oxygen-containing functional groups on the graphene surface can induce a larger charge transfer (ΔQ) from the polysulfide (S_3^- and S_3^{2-}) anions to graphene. For instance, the calculated ΔQ from S_3^- (S_3^{2-}) to HO-graphene increases from 0.4 (1.1) to 0.73 (1.4) electron, as shown in Figure 4c and d. Therefore, the increased binding effect can be ascribed to the larger ΔQ between S_3^- (S_3^{2-}) and graphene due to the existence of epoxide or hydroxyl groups on the graphene surface. It was also found that the HO-graphene shows stronger binding effects on the polysulfide (S_3^- and S_3^{2-}) anions than does the EO-graphene, and the binding energies are calculated to be 1.09 (1.95) eV and 0.84 (1.81) eV for S_3^- (S_3^{2-}) on the HO-graphene and EO-graphene, respectively. This mainly results from the fact that hydroxyl groups on the graphene surface can induce an asymmetrical charge distribution on the two end sulfur atoms of a S_3 cluster, resulting in larger polarization and consequently stronger electrostatic interaction between a S_3 cluster and the HO-graphene. Here, taking S_3^{2-} on the HO-graphene as an example, a larger partial charge (0.48 electron) for the end sulfur atom closer to the hydroxyl group than that (0.27 electron) for the sulfur atom at the other end is observed, as shown in Figure 4d.

In order to demonstrate the structural benefits of G−S hybrids and the bonding between graphene and sulfur nanocrystals for improving cathode performance, a series of electrochemical measurements were carried out. The G−S hybrids were cut into slices, compressed, and shaped into circular pellets, and then directly used as electrodes with high electrical conductivity (Figure S9). Cyclic voltammetry (CV) was used to reveal the

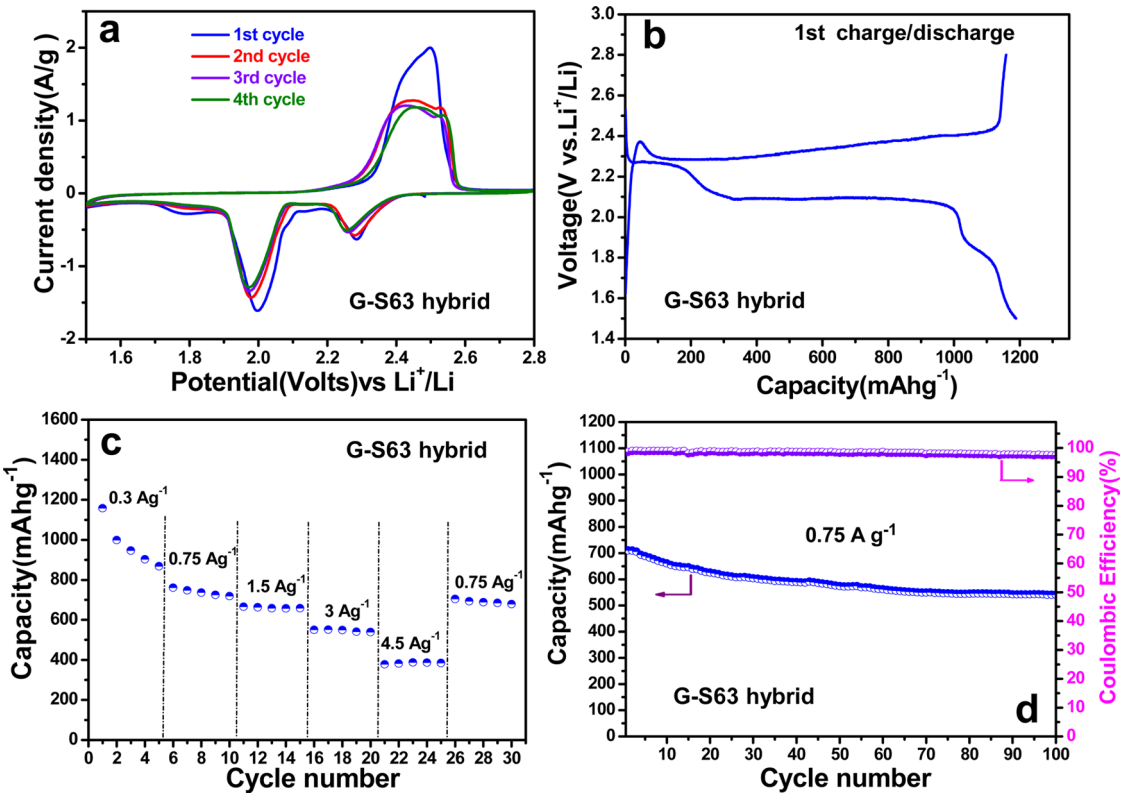

Figure 5. (a) CVs of the G−S63 cathode at 0.1 mV s^{-1} in a potential window from 1.5 to 2.8 V *vs* Li^+/Li^0. (b) First galvanostatic charge−discharge curves of the G−S63 cathode at 0.3 A g^{-1}. (c) Capacity at different current densities of the G−S63 cathode. (d) Cyclic performance and Coulombic efficiency of the G−S63 cathode at 0.75 A g^{-1} for 100 cycles after the high current density test.

electrochemical reaction mechanism of the G−S cathode measured between 1.5 and 2.8 V at a sweep rate of 0.1 mV s^{-1}, as shown in Figure 5a. During the first cathodic reduction process, three peaks at approximately 2.3, 2.0, and 1.8 V (*vs* Li^+/Li^0) were observed. The peak at 2.3 V corresponds to the reduction of sulfur to higher-order polysulfides (Li_2S_x, $4 < x < 8$).[6] The peaks at 2.0 and 1.8 V are related to the reduction of higher-order polysulfides to lower-order polysulfides (such as Li_2S_4, Li_2S_3, Li_2S_2) and Li_2S.[30,42] In the subsequent anodic scan, one asymmetric oxidation peak (which can be divided into two peaks) is observed at about 2.5 V and is attributed to the conversion of lithium sulfides to polysulfides and sulfur. These results are in agreement with galvanostatic charge−discharge curves (Figure 5b) and similar to other reports.[6,13,30,42] From the second cycle, both the CV peak positions and areas remain almost unchanged, suggesting relatively good capacity retention.

The rate capability of the G−S63 cathode is shown in Figure 5c, measured using a coin cell configuration with a lithium metal anode. The G−S63 cathode can deliver a capacity of 1160 mA h g^{-1} at 0.3 A g^{-1}, and the overall capacity of the cathode (including sulfur and graphene) is 731 mA h g^{-1}, calculated using the known sulfur weight ratio. The capacity of the G−S63 hybrid can be maintained at ~700 mA h g^{-1} after 50 cycles, much higher than those of the G−S59 hybrid (powder) with ~410 mA h g^{-1} and G−S60 hybrid (powder) with ~350 mA h g^{-1} after 50 cycles (Figure S10a). The sulfur content can be easily tuned by the initial sulfur addition, and the properties of G−S55 and G−S71 cathodes were compared in Figure S11a. With the increase of the current density to 1.5 and 4.5 A g^{-1}, the specific capacity of the G−S63 cathode is 670 and 390 mA h g^{-1} with the overall capacity of 422 and 246 mA h g^{-1}, demonstrating a high rate performance. Moreover, the material recovered most of the original capacity when the cycling current was restored to 0.75 A g^{-1}, implying that the structure of the sulfur electrode remains stable even under high rate cycling. The high rate performance of the G−S cathodes is attributed to the thin graphene and nanosized sulfur, which lead to short Li^+ diffusion distances, while the open porous structure provides rapid ion transport pathways. The immobilization of sulfur/(poly)sulfides by oxygen-containing groups during cycling is vitally important for the stable utilization of sulfur in the cathodes based on first-principles calculations, which is also verified by the existing S−O species in the S 2p region after being discharged to the end of the second plateau (Figure S12). As demonstrated in Figure 5d, the sulfur cathode can maintain a capacity as high as 541 mA h g^{-1} at 0.75 A g^{-1} for the G−S63 over 100 cycles even after the rate capability test, much better than those of G−S hybrids

(powder), as shown in Figure S10b. Furthermore, its Coulombic efficiency is around 98% for all the G–S cathodes during cycling (Figure 5d and Figure S11b). It should be noted that the entrapment of sulfur by the large surface areas and many functional groups of the graphene ensures a complete redox process, prevents sulfur from dissolving into the electrolyte, and results in improved cycling performance. Nonetheless, capacity degradation still occurs to some extent on repeated long-term cycling of the batteries, especially in the high sulfur sample, because the binding is not 100% efficient. Therefore, this and other strategies such as conductive polymer coating[1,43,44] and pore confinement[1,10,45] may be combined to further improve the performance of the G–S cathodes.

CONCLUSIONS

We have designed and prepared fibrous G–S hybrids by a one-pot reduction–assembly method, which is simple, highly efficient, and scalable. The G–S hybrids can be cut and pressed into Li–S battery electrodes without using a metal current-collector, polymeric binder, and conductive additive. The combination of the highly conductive interwoven fibrous graphene and the small size of the sulfur (5–10 nm) greatly improves the kinetics of charge and ion transfer in these G–S hybrid electrodes. Moreover, the strong absorption and interaction of oxygen-containing functional groups on graphene with sulfur/polysulfides effectively reduce the dissolution of polysulfide intermediates into the electrolyte and improve the cycling performance. DFT calculations reveal that the performance improvement results from the strong binding between the oxygen-containing functional groups on the graphene and sulfur/polysulfides, which reduces the irreversible loss of sulfur during discharge/charge. Therefore, the G–S hybrid cathodes demonstrate excellent electrochemical performance with high specific capacity, good rate performance, and stable cyclability over 100 cycles. These results demonstrate that these G–S hybrid cathodes are very promising candidates for high-performance Li–S batteries.

EXPERIMENTAL SECTION

Synthesis of GO. GO was synthesized from natural flake graphite by a modified Hummers' method.[46] The concentration of the GO suspension obtained was 1.8 mg mL^{-1}, which was determined by drying the suspension at 90 °C under vacuum for 24 h and then weighing the dried GO.

Synthesis of Intercalation-Exfoliated Graphene. Intercalation-exfoliated graphene powder was fabricated by Sichuan Jinlu Group Co., Ltd. using a solid-state intercalation and liquid-phase expansion and exfoliation method and was used as-received in this work.

Synthesis of the Thermally Exfoliated Reduced Graphene. Thermally exfoliated reduced graphene was prepared as reported in our previous work.[47]

Preparation of G–S Hybrids. G–S hybrids were prepared by hydrothermal reduction–assembly of GO with a sulfur-dissolving CS_2 and alcohol solution. In brief, 50 mL of the GO aqueous dispersion and 15 mL of alcohol were mixed, and then 3 mL of CS_2 containing 100, 150, and 200 mg of dissolved sulfur (tuning the sulfur content in the samples) was added to the GO dispersion. The mixture was stirred for 90 min and then sealed in an 80 mL Teflon-lined stainless steel autoclave for a hydrothermal reaction at 180 °C for 10 h. The black cylinder of the G–S hydrogel was washed by ethanol and distilled water, and the wet hydrogel was then freeze-dried to obtain the G–S hybrids.

Preparation of G–S Hybrids (Powder). G–S hybrids (powder) were prepared by mixing 90 mg of intercalation-exfoliated graphene and thermally exfoliated reduced graphene with 150 mg of sulfur under the same hydrothermal conditions as the G–S hybrids.

Preparation of G–S_{mix}. The G–S_{mix} was prepared by mixing 50 mL of the GO aqueous dispersion, 15 mL of alcohol, and 150 mg of sulfur under the same conditions but without CS_2.

Materials Characterization. SEM observations were carried out on an FEI Nova NanoSEM 430 at 15 kV. TEM and STEM were performed using a Tecnai F20 (200 kV). EDS was used for elemental analysis. XPS analysis was performed by using an ESCALAB 250 instrument with Al Kα radiation (15 kV, 150 W) under a pressure of 4×10^{-8} Pa. XRD was conducted with a D-MAX/2400 diffractometer (Cu Kα, $\lambda = 0.154056$ nm). TGA was performed with a NETZSCH STA 449C thermobalance in argon with a heating rate of 10 °C min^{-1} to 500 °C. The electrical conductivity of the electrodes was measured by a standard four-point probe resistivity measurement system (RTS-9, Guangzhou, China). Three measurements were carried out at different positions on each sample, and the average value was taken.

Electrochemical Measurements. The G–S hybrid was cut, compressed, and shaped into a circular pellet with a diameter of 12 mm and directly used as a cathode. The mass loading of a G–S electrode was about 2 mg cm^{-2}. The G–S59 or G–S60 hybrid (powder) cathode was prepared by mixing 90 wt % G–S59 or G–S60 hybrid (powder) with 10 wt % polyvinylidene fluoride dissolved in *N*-methyl-2-pyrrolidone as a binder to form a slurry, which was then coated on an aluminum foil and dried under vacuum at 70 °C for 12 h. The foil was pressed between twin rollers, shaped into a circular pellet with a diameter of 12 mm, and used as a cathode. The electrolyte was 1.0 M lithium bis-trifluoromethanesulfonylimide in 1,3-dioxolane and 1,2-dimethoxyethane (1:1 by volume) with 0.5 wt % $LiNO_3$ additive.[48] A 2025 type stainless steel coin cell was used to assemble a test cell. A lithium metal foil was used as the anode, and a G–S slice as the cathode. A LAND galvanostatic charge–discharge instrument was used to perform the measurements. The coin-type cell was assembled in an Ar-filled glovebox (MBraun Unilab). The current density set for cell tests was referred to the mass of sulfur in the cathode and varied from 0.3 to 4.5 A g^{-1}. The charge–discharge voltage range was 1.5–2.8 V. The CV was measured using a VSP-300 multichannel potentiostat/galvanostat (Bio-Logic, France) workstation in the voltage range 1.5–2.8 V (*vs* Li^+/Li) at a scan rate of 0.1 mV s^{-1}. The G–S63 hybrid electrode was discharged to the end of the second plateau and disassembled, dried in the glovebox, and followed by transferring to the vacuum chamber of XPS for structure characterization.

Theoretical Calculations. All calculations were performed with the plane-wave-based VASP code,[49,50] applying projector augmented wave (PAW)[51] pseudopotentials to describe electron–ion interactions, and the local density approximation functional (LDA)[52] for the electronic exchange correlation effect. Kohn–Sham one-electron valence states were expanded on the basis of plane waves with a cutoff energy of 400 eV. A large polyaromatic hydrocarbon (PAH) molecule consisting of 54 C atoms and 18 H atoms was constructed to represent the graphene within a cubic supercell (20 Å × 20 Å × 20 Å), as shown in Figure 4. The graphene oxide with hydroxyl (epoxide) groups was modeled by adding two OH groups (four O atoms) on both

sides of the PAH surface. The *k*-space sampling was restricted to the Γ-point for all calculations. All atomic positions were relaxed to a force convergence of 10^{-2} eV/Å, and a dipole correction[53] to the total energy was used to improve the energy convergence for charged systems. For an isolated S_3^- anion, the vertical detachment energy is calculated to be 2.47 eV, which is slightly less than the previously determined theoretical results (2.64 eV) and well reproduces the experimental value (2.50 eV).[39] The charge population was calculated using Bader charge analysis.[54]

Conflict of Interest: The authors declare no competing financial interest.

Acknowledgment. This work was supported by MOST (2011CB932604) and National Science Foundation of China (Nos. 50921004 and 51172239). We acknowledge the support from the Shenyang Supercomputing Center, CAS, China. D.W.W. acknowledges the support of a University of Queensland Foundation Research Excellence Award.

Supporting Information Available: Figures S1–S12. This information is available free of charge *via* the Internet at http://pubs.acs.org.

REFERENCES AND NOTES

1. Ji, X. L.; Lee, K. T.; Nazar, L. F. A Highly Ordered Nanostructured Carbon-Sulphur Cathode for Lithium-Sulphur Batteries. *Nat. Mater.* **2009**, *8*, 500–506.
2. Ellis, B. L.; Lee, K. T.; Nazar, L. F. Positive Electrode Materials for Li-Ion and Li-Batteries. *Chem. Mater.* **2010**, *22*, 691–714.
3. Bruce, P. G.; Freunberger, S. A.; Hardwick, L. J.; Tarascon, J.-M. Li-O_2 and Li-S Batteries with High Energy Storage. *Nat. Mater.* **2012**, *11*, 19–29.
4. Ji, X. L.; Nazar, L. F. Advances in Li-S Batteries. *J. Mater. Chem.* **2010**, *20*, 9821–9826.
5. Scrosati, B.; Hassoun, J.; Sun, Y. K. Lithium-Ion Batteries. A Look into the Future. *Energy Environ. Sci.* **2011**, *4*, 3287–3295.
6. Xiao, L. F.; Cao, Y. L.; Xiao, J.; Schwenzer, B.; Engelhard, M. H.; Saraf, L. V.; Nie, Z. M.; Exarhos, G. J.; Liu, J. A Soft Approach to Encapsulate Sulfur: Polyaniline Nanotubes for Lithium-Sulfur Batteries with Long Cycle Life. *Adv. Mater.* **2012**, *24*, 1176–1181.
7. Schuster, J.; He, G.; Mandlmeier, B.; Yim, T.; Lee, K. T.; Bein, T.; Nazar, L. F. Spherical Ordered Mesoporous Carbon Nanoparticles with High Porosity for Lithium–Sulfur Batteries. *Angew. Chem., Int. Ed.* **2012**, *51*, 3591–3595.
8. Liang, C. D.; Dudney, N. J.; Howe, J. Y. Hierarchically Structured Sulfur/Carbon Nanocomposite Material for High-Energy Lithium Battery. *Chem. Mater.* **2009**, *21*, 4724–4730.
9. Lai, C.; Gao, X. P.; Zhang, B.; Yan, T. Y.; Zhou, Z. Synthesis and Electrochemical Performance of Sulfur/Highly Porous Carbon Composites. *J. Phys. Chem. C* **2009**, *113*, 4712–4716.
10. Zhang, B.; Qin, X.; Li, G. R.; Gao, X. P. Enhancement of Long Stability of Sulfur Cathode by Encapsulating Sulfur into Micropores of Carbon Spheres. *Energy Environ. Sci.* **2010**, *3*, 1531–1537.
11. Jayaprakash, N.; Shen, J.; Moganty, S. S.; Corona, A.; Archer, L. A. Porous Hollow Carbon@Sulfur Composites for High-Power Lithium-Sulfur Batteries. *Angew. Chem., Int. Ed.* **2011**, *50*, 5904–5908.
12. Zhang, C.; Wu, H. B.; Yuan, C.; Guo, Z.; Lou, X. W. Confining Sulfur in Double-Shelled Hollow Carbon Spheres for Lithium–Sulfur Batteries. *Angew. Chem., Int. Ed.* **2012**, *51*, 9456–9456.
13. Guo, J. C.; Xu, Y. H.; Wang, C. S. Sulfur-Impregnated Disordered Carbon Nanotubes Cathode for Lithium-Sulfur Batteries. *Nano Lett.* **2011**, *11*, 4288–4294.
14. Zheng, G. Y.; Yang, Y.; Cha, J. J.; Hong, S. S.; Cui, Y. Hollow Carbon Nanofiber-Encapsulated Sulfur Cathodes for High Specific Capacity Rechargeable Lithium Batteries. *Nano Lett.* **2011**, *11*, 4462–4467.
15. Cao, Y. L.; Li, X. L.; Aksay, I. A.; Lemmon, J.; Nie, Z. M.; Yang, Z. G.; Liu, J. Sandwich-Type Functionalized Graphene Sheet-Sulfur Nanocomposite for Rechargeable Lithium Batteries. *Phys. Chem. Chem. Phys.* **2011**, *13*, 7660–7665.
16. Wang, H. L.; Yang, Y.; Liang, Y. Y.; Robinson, J. T.; Li, Y. G.; Jackson, A.; Cui, Y.; Dai, H. J. Graphene-Wrapped Sulfur Particles as a Rechargeable Lithium-Sulfur Battery Cathode Material with High Capacity and Cycling Stability. *Nano Lett.* **2011**, *11*, 2644–2647.
17. Zhao, M.-Q.; Liu, X.-F.; Zhang, Q.; Tian, G.-L.; Huang, J.-Q.; Zhu, W.; Wei, F. Graphene/Single-Walled Carbon Nanotube Hybrids: One-Step Catalytic Growth and Applications for High-Rate Li–S Batteries. *ACS Nano* **2012**, *6*, 10759–10769.
18. Huang, J.-Q.; Liu, X.-F.; Zhang, Q.; Chen, C.-M.; Zhao, M.-Q.; Zhang, S.-M.; Zhu, W.; Qian, W.-Z.; Wei, F. Entrapment of Sulfur in Hierarchical Porous Graphene for Lithium–Sulfur Batteries with High Rate Performance from −40 to 60°C. *Nano Energy* **2013**, *2*, 314–321.
19. Bai, H.; Li, C.; Shi, G. Functional Composite Materials Based on Chemically Converted Graphene. *Adv. Mater.* **2011**, *23*, 1089–1115.
20. Wu, Z.-S.; Zhou, G. M.; Yin, L.-C.; Ren, W.; Li, F.; Cheng, H.-M. Graphene/Metal Oxide Composite Electrode Materials for Energy Storage. *Nano Energy* **2012**, *1*, 107–131.
21. Segal, M. Selling Graphene by the Ton. *Nat. Nanotechnol.* **2009**, *4*, 611–613.
22. Yang, X. W.; Zhu, J. W.; Qiu, L.; Li, D. Bioinspired Effective Prevention of Restacking in Multilayered Graphene Films: Towards the Next Generation of High-Performance Supercapacitors. *Adv. Mater.* **2011**, *23*, 2833–2838.
23. Li, C.; Shi, G. Q. Three-Dimensional Graphene Architectures. *Nanoscale* **2012**, *4*, 5549–5563.
24. Qiu, L.; Liu, J. Z.; Chang, S. L. Y.; Wu, Y.; Li, D. Biomimetic Superelastic Graphene-Based Cellular Monoliths. *Nat. Commun.* **2012**, *3*, 1241.
25. Choi, B. G.; Yang, M.; Hong, W. H.; Choi, J. W.; Huh, Y. S. 3D Macroporous Graphene Frameworks for Supercapacitors with High Energy and Power Densities. *ACS Nano* **2012**, *6*, 4020–4028.
26. Chen, W. F.; Li, S. R.; Chen, C. H.; Yan, L. F. Self-Assembly and Embedding of Nanoparticles by *in Situ* Reduced Graphene for Preparation of a 3D Graphene/Nanoparticle Aerogel. *Adv. Mater.* **2011**, *23*, 5679–5683.
27. Xu, Y. X.; Sheng, K. X.; Li, C.; Shi, G. Q. Self-Assembled Graphene Hydrogel *via* a One-Step Hydrothermal Process. *ACS Nano* **2010**, *4*, 4324–4330.
28. Mukherjee, R.; Thomas, A. V.; Krishnamurthy, A.; Koratkar, N. Photothermally Reduced Graphene as High-Power Anodes for Lithium-Ion Batteries. *ACS Nano* **2012**, *6*, 7867–7878.
29. Demir-Cakan, R.; Morcrette, M.; Nouar, F.; Davoisne, C.; Devic, T.; Gonbeau, D.; Dominko, R.; Serre, C.; Ferey, G.; Tarascon, J. M. Cathode Composites for Li-S Batteries *via* the Use of Oxygenated Porous Architectures. *J. Am. Chem. Soc.* **2011**, *133*, 16154–16160.
30. Ji, L. W.; Rao, M. M.; Zheng, H.; Zhang, L.; Li, Y.; Duan, W.; Guo, J.; Cairns, E. J.; Zhang, Y. Graphene Oxide as a Sulfur Immobilizer in High Performance Lithium/Sulfur Cells. *J. Am. Chem. Soc.* **2011**, *133*, 18522–18525.
31. Zhang, L.; Ji, L.; Glans, P.-A.; Zhang, Y.; Zhu, J.; Guo, J. Electronic Structure and Chemical Bonding of a Graphene Oxide-Sulfur Nanocomposite for Use in Superior Performance Lithium-Sulfur Cells. *Phys. Chem. Chem. Phys.* **2012**, *14*, 13670–13675.
32. Zhou, G. M.; Wang, D.-W.; Yin, L.-C.; Li, N.; Li, F.; Cheng, H.-M. Oxygen Bridges between NiO Nanosheets and Graphene for Improvement of Lithium Storage. *ACS Nano* **2012**, *6*, 3214–3223.
33. Wu, Z. S.; Wang, D. W.; Ren, W.; Zhao, J.; Zhou, G.; Li, F.; Cheng, H. M. Anchoring Hydrous RuO_2 on Graphene Sheets for High-Performance Electrochemical Capacitors. *Adv. Funct. Mater.* **2010**, *20*, 3595–3602.
34. Stankovich, S.; Dikin, D. A.; Piner, R. D.; Kohlhaas, K. A.; Kleinhammes, A.; Jia, Y.; Wu, Y.; Nguyen, S. T.; Ruoff, R. S. Synthesis of Graphene-Based Nanosheets *via* Chemical Reduction of Exfoliated Graphite Oxide. *Carbon* **2007**, *45*, 1558–1565.

35. Lv, W.; Tang, D. M.; He, Y. B.; You, C. H.; Shi, Z. Q.; Chen, X. C.; Chen, C. M.; Hou, P. X.; Liu, C.; Yang, Q. H. Low-Temperature Exfoliated Graphenes: Vacuum-Promoted Exfoliation and Electrochemical Energy Storage. *ACS Nano* **2009**, *3*, 3730–3736.
36. Zhang, G. X.; Sun, S. H.; Yang, D. Q.; Dodelet, J. P.; Sacher, E. The Surface Analytical Characterization of Carbon Fibers Functionalized by H_2SO_4/HNO_3 Treatment. *Carbon* **2008**, *46*, 196–205.
37. Schaufuß, A. G.; Nesbitt, H. W.; Kartio, I.; Laajalehto, K.; Bancroft, G. M.; Szargan, R. Incipient Oxidation of Fractured Pyrite Surfaces in Air. *J. Electron Spectrosc. Relat. Phenom.* **1998**, *96*, 69–82.
38. Bagri, A.; Mattevi, C.; Acik, M.; Chabal, Y. J.; Chhowalla, M.; Shenoy, V. B. Structural Evolution during the Reduction of Chemically Derived Graphene Oxide. *Nat. Chem.* **2010**, *2*, 581–587.
39. Hunsicker, S.; Jones, R. O.; Gantefor, G. Rings and Chains in Sulfur Cluster Anions S^- to S_9^- Theory (Simulated Annealing) and Experiment (Photoelectron Detachment). *J. Chem. Phys.* **1995**, *102*, 5917–5936.
40. Berghof, V.; Sommerfeld, T.; Cederbaum, L. S. Sulfur Cluster Dianions. *J. Phys. Chem. A* **1998**, *102*, 5100–5105.
41. Xin, S.; Gu, L.; Zhao, N.-H.; Yin, Y.-X.; Zhou, L.-J.; Guo, Y.-G.; Wan, L.-J. Smaller Sulfur Molecules Promise Better Lithium−Sulfur Batteries. *J. Am. Chem. Soc.* **2012**, *134*, 18510–18513.
42. Zhou, G. M.; Wang, D.-W.; Li, F.; Hou, P.-X.; Yin, L.; Liu, C.; Lu, G. Q.; Gentle, I. R.; Cheng, H.-M. A Flexible Nanostructured Sulphur-Carbon Nanotube Cathode with High Rate Performance for Li-S Batteries. *Energy Environ. Sci.* **2012**, *5*, 8901–8906.
43. Yang, Y.; Yu, G. H.; Cha, J. J.; Wu, H.; Vosgueritchian, M.; Yao, Y.; Bao, Z. A.; Cui, Y. Improving the Performance of Lithium-Sulfur Batteries by Conductive Polymer Coating. *ACS Nano* **2011**, *5*, 9187–9193.
44. Zhang, S.-M.; Zhang, Q.; Huang, J.-Q.; Liu, X.-F.; Zhu, W.; Zhao, M.-Q.; Qian, W.-Z.; Wei, F. Composite Cathodes Containing SWCNT@S Coaxial Nanocables: Facile Synthesis, Surface Modification, and Enhanced Performance for Li-Ion Storage. *Part. Part. Syst. Charact.* **2013**, *30*, 158–165.
45. Wang, D.-W.; Zhou, G. M.; Li, F.; Wu, K.-H.; Lu, G. M.; Cheng, H.-M.; Gentle, I. A Microporous-Mesoporous Carbon with Graphitic Structure for a High-Rate Stable Sulfur Cathode in Carbonate Solvent-Based Li-S Batteries. *Phys. Chem. Chem. Phys.* **2012**, *14*, 8703–8710.
46. Zhao, J.; Pei, S.; Ren, W.; Gao, L.; Cheng, H.-M. Efficient Preparation of Large-Area Graphene Oxide Sheets for Transparent Conductive Films. *ACS Nano* **2010**, *4*, 5245–5252.
47. Wu, Z. S.; Ren, W. C.; Gao, L. B.; Liu, B. L.; Jiang, C. B.; Cheng, H. M. Synthesis of High-Quality Graphene with a Pre-Determined Number of Layers. *Carbon* **2009**, *47*, 493–499.
48. Aurbach, D.; Pollak, E.; Elazari, R.; Salitra, G.; Kelley, C. S.; Affinito, J. On the Surface Chemical Aspects of Very High Energy Density, Rechargeable Li-Sulfur Batteries. *J. Electrochem. Soc.* **2009**, *156*, A694–A702.
49. Kresse, G.; Furthmuller, J. Efficient Iterative Schemes for Ab Initio Total-Energy Calculations Using a Plane-Wave Basis Set. *Phys. Rev. B* **1996**, *54*, 11169–11186.
50. Kresse, G.; Furthmuller, J. Efficiency of Ab-Initio Total Energy Calculations for Metals and Semiconductors Using a Plane-Wave Basis Set. *Comput. Mater. Sci.* **1996**, *6*, 15–50.
51. Blochl, P. E. Projector Augmented-Wave Method. *Phys. Rev. B* **1994**, *50*, 17953–17979.
52. Perdew, J. P.; Zunger, A. Self-Interaction Correction to Density-Functional Approximations for Many-Electron Systems. *Phys. Rev. B* **1981**, *23*, 5048–5079.
53. Makov, G.; Payne, M. C. Periodic Boundary-Conditions in Ab-Initio Calculations. *Phys. Rev. B* **1995**, *51*, 4014–4022.
54. Henkelman, G.; Arnaldsson, A.; Jonsson, H. A Fast and Robust Algorithm for Bader Decomposition of Charge Density. *Comput. Mater. Sci.* **2006**, *36*, 354–360.